PHOTONIC SENSORS / Vol. 14, No. 1, 2024: 240122

Vertical Displacement Measurement in a Slow-Moving Sinkhole Using BOTDA

Pascual SEVILLANO[1*], Javier PRECIADO-GARBAYO[2,3], Jorge SEVIL[4],
Francisco GUTIÉRREZ[4], Juan J. MARTÍNEZ[3], Sonia MARTÍN-LÓPEZ[5],
and Miguel GONZÁLEZ-HERRÁEZ[5]

[1] *Aragon Institute of Engineering Research (I3A), Universidad de Zaragoza, Zaragoza 50018, Spain*

[2] *Electronic Engineering and Communications Department, EINA, Universidad de Zaragoza, Zaragoza 50018, Spain*

[3] *Aragon Photonics Labs., Zaragoza 50009, Spain*

[4] *Department of Earth Sciences, Universidad de Zaragoza, Zaragoza 50009, Spain*

[5] *Department of Electronics, Escuela Politécnica Superior, Universidad de Alcalá, Madrid 28805, Spain*

[*] Corresponding author: Pascual SEVILLANO E-mail: psevi@unizar.es

Abstract: The effectiveness of monitoring and early-warning systems for ground deformation phenomena, such as sinkholes, depends on their ability to accurately resolve the ongoing ground displacement and detect the subtle deformation preceding catastrophic failures. Sagging sinkholes with a slow subsidence rate and diffuse edges pose a significant challenge for subsidence monitoring due to the low deformation rates and limited lateral strain gradients. In this work, we satisfactorily illustrate the practicality of the Brillouin optical time domain analysis (BOTDA) to measure the spatial-temporal patterns of the vertical displacement in such challenging slow-moving sagging sinkholes. To assess the performance of the approach, we compare the strain recorded by the distributed optical fiber sensor with the vertical displacement measured by high-precision leveling. The results show a good spatial correlation with the ability to identify the maximum subsidence point. There is also a good temporal correlation with the detection of an acceleration phase in the subsidence associated with a flood event.

Keywords: Distributed fiber optic sensing (DFOS); vertical displacement measurement; slow subsidence rate; sinkhole hazard; early-warning system

Citation: Pascual SEVILLANO, Javier PRECIADO-GARBAYO, Jorge SEVIL, Francisco GUTIÉRREZ, Juan J. MARTÍNEZ, Sonia MARTÍN-LÓPEZ, *et al.*, "Vertical Displacement Measurement in a Slow-Moving Sinkhole Using BOTDA," *Photonic Sensors*, 2024, 14(1): 240122.

1. Introduction

Distributed optical fiber sensors (DOFSs) have been proved to be a useful tool for measuring spatial and temporal variations in strain and temperature along man-made structures, such as dams, bridges, and tunnels [1–4]. The analysis of the scattered light that travels along the fiber can reveal mechanical and thermal perturbations in the region, where the fiber has been deployed. The sensing optical fiber is often deployed in natural hostile environments capturing external information that is conveyed into the optical domain. The interrogator together with the electronics required for collecting the data is placed at the end of the fiber within a more stable and secure environment. The range, resolution, and

---

Received: 3 March 2023 / Revised: 24 August 2023

DOI: 10.1007/s13320-023-0696-7
Article type: Regular

bandwidth are the key parameters that determine the applicability of the different optical fiber sensor technologies.

Among the DOFSs, those based on the Brillouin scattering make use of a highly coherent laser to generate non-linear scattering and analyze its spatial-temporal changes. In these systems, a fraction of the incident light is backscattered towards the emitter with a characteristic frequency shift, named the Brillouin frequency shift (BFS) [5]. Initially, the analysis of the distributed Brillouin scattering was proposed as an alternative technology for characterizing fiber parameters, such as the attenuation coefficient [6]. However, soon it was demonstrated that this method also allows the measurement of other parameters. In the Brillouin time domain analysis (BOTDA) scheme, two counter-propagating waves are coupled into the system, stimulating the scattering and producing the so-called stimulated Brillouin scattering (SBS). The local BFS is strongly dependent on the mechanical and thermal conditions of the fiber. Consequently, by resolving the distributed frequency shift of the scattering process, we can monitor variations in strain and temperature along the fiber. The use of BOTDA for monitoring the linear infrastructure has been widely reported because of its practicality for accurately measuring temperature and static strain along long distances. In its most common set-up, the technology allows collecting measurements along tens of kilometers with a meter-scale resolution and a sensitivity of tens of $\mu\varepsilon$ [7]. The possibility of using the conventional single-mode fiber, including those already deployed in communication links or other common configurations, has positioned this technique as a very appealing option for monitoring deformations related to multiple processes in the critical civil infrastructure [8].

Ground subsidence can cause severe damage to any human structure. Moreover, catastrophic subsidence involving the sudden occurrence of collapse sinkholes can also result in human life losses [9]. For instance, unforeseen subsidence impinging on a high-speed railway can lead to disastrous consequences. Subsidence phenomena dominated by the vertical ground displacement can be related to multiple natural and anthropogenic processes, such as the dissolution of soluble rocks, thawing of ground ice in permafrost regions, the collapse of lava tubes, internal erosion of fine-grained sediments (piping), aquitard consolidation induced by groundwater withdrawal, or the foundering of mine roofs. Critical data for mitigating the economic and societal risk related to subsidence impacting on human structures include: 1) identifying and delimiting the areas affected by active deformation; 2) measuring subsidence rates and characterizing their spatial-temporal patterns; 3) detecting deformation preceding catastrophic collapse (precursory subsidence) for the implementation of early-warning systems. The development of new monitoring techniques that allow gathering automatically distributed stain data with the high accuracy and along long distances is opening new possibilities for subsidence risk management. One of such techniques is the DOFS that features a number of strengths, including its non-destructive nature, capability for long-distance monitoring, electromagnetic immunity, water and corrosion resistance, and durability. In particular, the performance of the BOTDA technique for subsidence monitoring has been tested in recent years either in laboratory conditions or in artificially created sinkholes. In those artificial scenarios where the BOTDA has been tested, specially designed fibers are deployed to measure large vertical displacements of the order of tens of centimeters, without assessing its sensitivity and capability for detecting slow ground movements that could anticipate the catastrophic collapse.

In this work, we present the results of a BOTDA measurement system installed in a damaging sinkhole related to the salt dissolution that affects a flood-control embankment at Alcalá de Ebro village [Alcalá de Ebro, north east (NE) Spain], creating a high-risk and uncertain situation. This sinkhole, characterized by very slow sagging subsidence, shows temporal variations in the subsidence rate controlled by the flood regime and the associated changes in the position of the water table. The strain data obtained with an enhanced BOTDA sensor interrogating off-the-shelf optical fiber cables are compared with the subsidence data measured by high-precision leveling (HPL) at the same site. The comparison between the spatial and temporal patterns of the displacement measured by both methods allows assessing independently, quantitatively, and for the first time the performance of the BOTDA technique for the sinkhole subsidence measurement using a real sinkhole under natural conditions.

2. Case of Study

2.1 High-risk Alcalá sinkhole

The Alcalá de Ebro village is located in the floodplain of the Ebro River in NE Spain, adjoining the outer side of a meander (Fig. 1). Here, the 6 m–7 m thick alluvium is underlain in descending order by a dissolution residue up to 20 m thick made up of the dark clay and marl with the residual gypsum, and a subhorizontally-lying Miocene evaporitic bedrock including halite and glauberite beds (equilibrium solubilities of 356 g/L and 118 g/L, respectively). Data from boreholes drilled at the sinkhole site indicate a high frequency of meter-sized cavities at depths between 13 m and 19 m. The Alcalá sinkhole is a diffuse-edged sagging sinkhole around 100 m across that has been affected by multiple nested catastrophic collapses since 2007, creating high-risk situations because of the potential for a dike failure during a flood [Fig. 1(c)]. Previous monitoring data collected by the high-precision leveling and terrestrial laser scanner reveal phases of accelerated subsidence associated with flood events that have an immediate response on the position of the water table. Further information on the geology, subsidence history, and remediation measures applied can be found in [10].

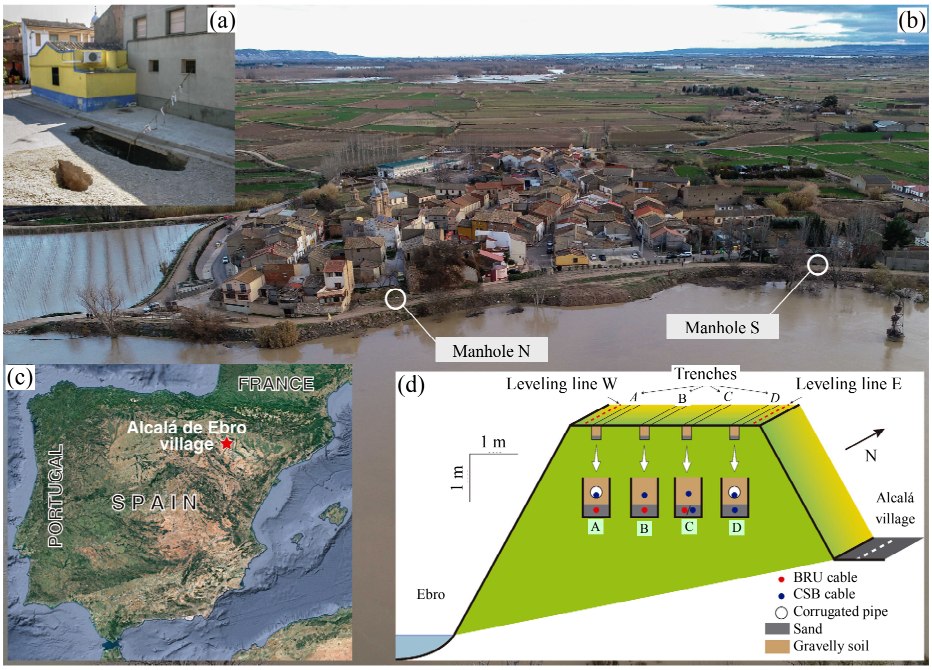

Fig. 1 Location of the Alcalá de Ebro sinkhole and monitoring layout: (a) nested collapse occurred in July 2007 in the street, undermining a house which was subsequently demolished, (b) oblique aerial view of Alcalá de Ebro village on the outer side of a meander and protected by a flood-control dike (the sinkhole, situated between the two manholes, affects the dike and an adjacent portion of the village; the image was taken during the December 2021 Ebro River flood), (c) location of Alcalá de Ebro village in NE Spain, and (d) sketch illustrating the distribution of the leveling lines and the different types of fiber cables installed in the four trenches excavated along the crest of the dike. S: south; W: west.

2.2 Fiber deployment and reference monitoring

The fiber cables are installed in four parallel trenches excavated along a 136 m long section of the dike crest [Fig. 1(d)]. The 0.4 m wide and 0.6 m deep backhoe trenches have a lateral separation of around 1.2 m and their traces at both extremes bend eastward and merge into a single trench connected to Manholes N and S in the north and south, respectively. From west (river side) to east (village side), the trenches are designated as A, B, C, and D. Two cables are deployed in each trench: one of them is referred to its commercial name BRU and the other one is referred to CSB. Both cables present a tight-buffer structure that ensures the mechanical transmission of the stress from the outer layer of the cable to the inner fiber, while preventing the damage potentially caused by the surrounding environment.

The cables are distinguished solely by the outer armor, which for the BRU cable is made of fiberglass braid, while the armor in the CSB is made of the corrugated steel. Having comparable constituents within their inner structure, they exhibit analogous mechanical and thermal responsiveness. The inner structure of both cables is depicted in Fig. 2, where the material of the layers is indicated. Each cable has 4 separated single-mode fibers evenly spaced around the center.

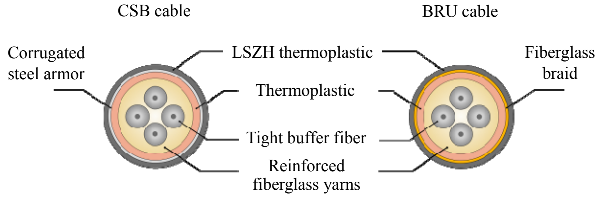

Fig. 2 Internal structure and elements of the deployed cables named BRU and CSB. LSZH stands for low smoke zero halogen.

The cables are laid at different depths. The bottom cables are embedded within a 20 cm thick fill of the well-graded sand. The upper cables are placed within a gravelly fill derived from the excavation of the trenches. The BRU cable is placed at the bottom of Trenches A, B, and C, and the CSB cable at the bottom of Trenches C and D and the upper level of all the trenches. Note that the bottom of Trench C has both BRU and CSB connected with a splice due to the insufficient supply of the former cable (Fig. 3). The upper-level CSB cables in Trenches A and D are placed within a pipe to prevent strain effects and isolate the temperature signal. The layout of the fiber cables with respect to the trenches and manholes is shown in Fig. 3. The figure shows the optical path of the pulse along the system for one round. For each round, the fiber end is spliced to the starting end of the next round in Manhole N, then creating a 4-round loop following the layout depicted in Fig. 3.

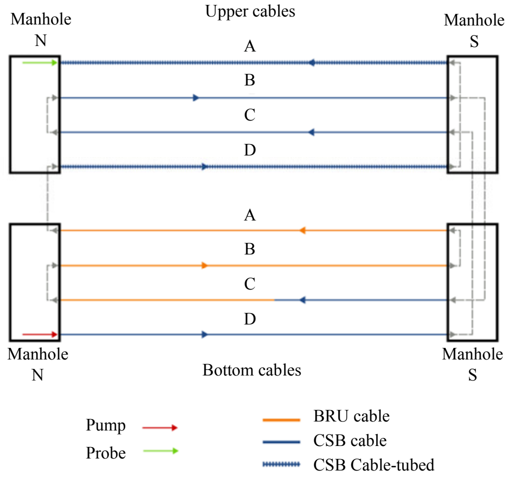

Fig. 3 Layout of the fiber cables buried at two depths denoted as upper cables and bottom cables. The arrows indicate the direction of the pulse travelling along the fiber.

Two leveling lines 136 m long with the 8 m spacing between benchmarks are installed at the edges of the dike crest, coinciding with the section of the dike monitored with the optical fiber. Leveling Line W adjoins Trench A on the river side and leveling Line E lies next to Trench D on the village side (Fig. 1). The nine leveling campaigns cover a time period of 736 days, spanning from 19 May 2020 to 25 May 2022, with measurements taken around every three months. This measurement period includes an ordinary flood that peaked on 14 December 2021.

Despite the investigated section of the dike being restricted to traffic, some benchmarks were found damaged in the campaigns of 22 September 2021 and 20 December 2021. The benchmarks were replaced to re-establish measurements in the following campaigns. The vertical ground displacement was measured by high-precision leveling using a digital level (Leica DNA03) mounted on a tripod with fixed-length legs, and a 2 m long bar-coded invar staff (Leica GPCL2). The utmost accuracy with a standard deviation of 0.3 mm per kilometer in double-run leveling could be achieved with this equipment. The measured values were considered invalid when the difference between the forward and backward measurements was higher than 0.3 mm. Profiles of the cumulative vertical displacement were plotted using the first profile as the datum and assuming that the benchmark situated at the initial edge of the line remains stable (see [10]) for additional details.

3. Measurement methodology

BOTDA techniques measure the BFS at every point of the fiber providing information on its physical status (i.e., strain and temperature). In its most fundamental implementation, the pump is pulsed and coupled into one end of the fiber, while the continuous probe is injected from the other end. The local interaction between the pump pulse and the counter-propagating probe wave induces a localized SBS amplification (from the pump over the probe). The temporal analysis of the amplified probe and its relationship with the propagation time of the pulse allows resolving the position of the measurements of the Brillouin gain along the fiber. Using the refractive index of the fiber and thus the velocity of the pulse, the recorded amplification of the probe can be correlated with the location of the pulse. The acquisition rate of the probe power determines the sampling spatial resolution of the system. In our case, with a rate of 100 MS/s, the sampling is set to 1 m. By recording the power level of the probe continuously, the system is able to sense variations of its value as the pump pulse travels through the fiber and interacts with the counter-propagating continuous probe. The gauge length of the pump-probe interaction is essentially limited to the segment of the fiber covered by the pulse, which is directly related to the temporal width of the pulse. In our case, the pump width is set to 20 ns, which corresponds to a resolution of 2 m. Sweeping the emission wavelength of the probe, the system characterizes the narrowband gain profile induced by the SBS at every point. The result is a distributed 3-dimentional (3D) map of the gain along the fiber. The enhanced accuracy in the determination of the central frequency of the gain profile (i.e., BFS) is usually obtained by fitting a Voight curve and interpolating its maximum gain frequency. Spatial and temporal changes in the BFS are a function of the strain and temperature variations experienced by the fiber and their corresponding dependence coefficients:

$$\Delta \nu_B = C_\varepsilon \Delta \varepsilon + C_T \Delta T . \tag{1}$$

The temperature coefficient for the single-mode fiber is $C_T = 1$ MHz/℃, while the strain coefficient, for the employed cables, has been evaluated in the lab within the range 0–40 ℃ and is in the order of the common value for the standard single-mode fiber, $C_\varepsilon = 0.05$ MHz/με [11–13]. In this scenario, we address the temperature-induced variations by using the BFS data obtained from the cables within the corrugated tubes. This compensation technique consists of subtracting the BFS value obtained in these strain-isolated cables from the BFS obtained in the directly buried cables, considering analogous temperature coefficients [14]. The presence of local hot spots in the terrain that could induce a temperature increase/decrease in specific locations is ruled out by analyzing the evolution of the BFS across the tubed fibers for different campaigns. It was found that the maximum difference in the BFS for the CSB-D tube occurred between the two extreme temperatures, i.e., December 2020 and June 2021 where it reached 0.6 MHz, corresponding to values below 1 ℃. This practically negligible temperature variation profile across the sinkhole is reasonable due to the limited extent of the layout and its homogeneity. This temperature compensation technique is widely used for isolating temperature and strain contributions to the BFS [15]. Based on these premises and data, the mean temperature variations between campaigns are compensated by assessing the average BFS variation along the cables positioned in the corrugated tubes and subtracting it from the BFS obtained in the cables directly buried in the terrain. Figure 4 shows, in the red line, the average BFS obtained from the section of the cables deployed within the corrugated tubes, while the blue line shows the average ambient temperature registered by a public domain weather station located 20 km apart from the site during the measurement lapse. Both lines exhibit a similar trend along the campaigns. This indicates that the measurements obtained in this section of the cable placed at the same depth of the other cables, can be used to discount the effect of surrounding temperature variations along different campaigns.

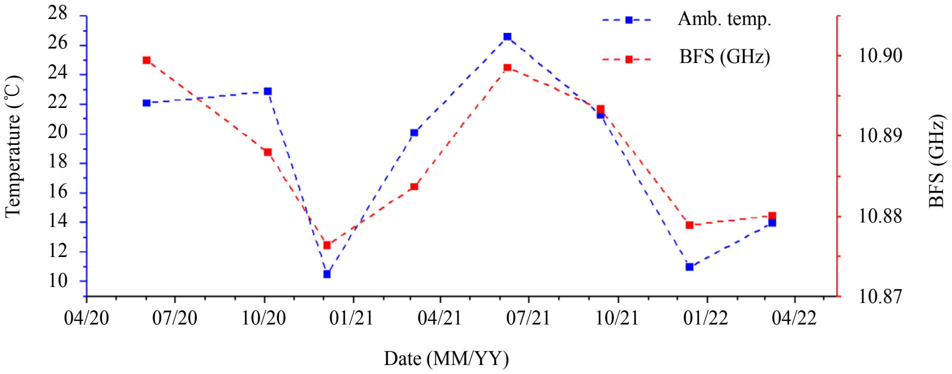

Fig. 4 Average BFS obtained in the section of the cable placed within the corrugated tubes (red) and average temperature during the measurement period (blue).

Nonetheless, resolving the relationship between elongation and potential changes in the position of the fiber related to ground instability phenomena is not straightforward. Some papers explore geometrical models for estimating the fiber/ground displacement related to landslides and sinkholes on the basis of the measured strain [16, 17]. An additional important factor for the displacement estimation is the coupling between the fiber cable and ground [18]. In situations in which the ground is affected by the substantial displacement, the position of the embedded cable will mimic the deformation experienced by the ground, serving as a reliable deformation marker [19]. However, in settings with low deformation rates as the one considered in this work, the fiber can exhibit the lower displacement than the surrounding material as it has been demonstrated in several works [18]. In situations with slow-moving sinkholes dominated by subsidence deformation, it can be assumed that the displacement of the fiber mainly has a vertical component for all points and measurement campaigns [20, 21]. In this case study, due to the slow subsidence rate and the unknown degree of coupling between the deployed fiber and the ground, we will consider the deformation of the fiber (ΔL) at each point x of the system as

$$\Delta L(x)=\int_0^x \varepsilon(l)\,\mathrm{d}l \tag{2}$$

where $\varepsilon(l)$ is the measured strain along the fiber [22]. Deformation is defined as the change in the length of the fiber and can be calculated with a space integration of the distributed strain as it is expressed in (2). Furthermore, where tensile extension is low, the non-negligible rigidity of the cable may play a role in the strain profile when the system is under tension. Those scenarios have been modeled by [23] and verified in subsequent works by [4]. Under these conditions, it can be considered that the relation between the strain and the vertical displacement is as follows:

$$\varepsilon \propto -\frac{1}{d}\frac{\partial^2 y}{\partial x^2} \tag{3}$$

where y is the vertical displacement at any point x of the fiber and d is the radius of the cable. Figure 5 displays how the magnitudes of displacement, deformation, and strain correlate for the local subsidence with a Gaussian shape. It shows that the maximum values of the displacement and strain are located in the same position, while it corresponds to an inflection point in the deformation graph. Additionally, the strain profile shows negative values in the central sector of the subsidence zone and positive values at the margins.

This behavior has been reproduced in the lab by [24], recording the strain profile for small vertical displacements. Consequently, the strain measured in the fiber can be considered as a proxy for the sinkhole-related subsidence, which can be compared with the measurements of the vertical ground displacement obtained by geodetic methods, such as high-precision leveling.

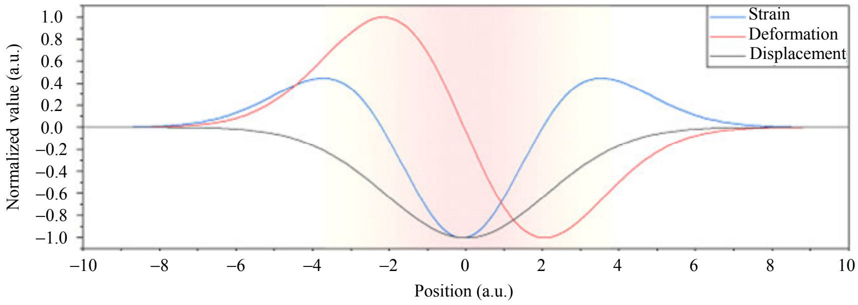

Fig. 5 Theoretical distribution of the strain, deformation, and displacement magnitudes associated with the Gaussian-shaped subsidence.

3.1 Repetitiveness

The BFS corresponds to the frequency difference between the pump and the probe when the amplification of the latter is the maximum. The frequency sweep range constrains the maximum absolute strain that the system is able to measure. The time needed for each measurement is strongly dependent on the frequency sweep configuration, and this trade-off must be considered when measuring rapid strain-related phenomena. The uncertainty of the measurements is related to the frequency sweep step and the curve fitting. There are several methods to reduce and assess the uncertainty of the measurements. In our case, the timescale of the strain variations is much greater than the measurement time and thus the uncertainty is reduced by averaging the BFS over several measurements for each campaign. Besides, the subsidence in the analyzed sinkhole is continuous rather than episodic [10, 25], reducing the uncertainty attributable to short-lasting changes in the strain. The capability of the system to measure strain and/or temperature in this application relies on its ability to measure variations of the spatially-resolved BFS between different measurement campaigns.

The characteristics of the sinkhole environment determine that the interrogator could not be permanently deployed on-site. Instead, it has to be installed and uninstalled in every measurement campaign. The device is designed and mounted in a solid box by the company Aragon Photonics Labs, which also programs the interface and measurement software, based on the architecture detailed in [26]. Measurements are taken by placing the system close to Manhole A (Fig. 1) to interrogate the fiber from this end. In each campaign, a set of 10 measurements are systematically taken between dawn and noon. A repeatability analysis of the data allows discarding those with higher noise and uncertainty.

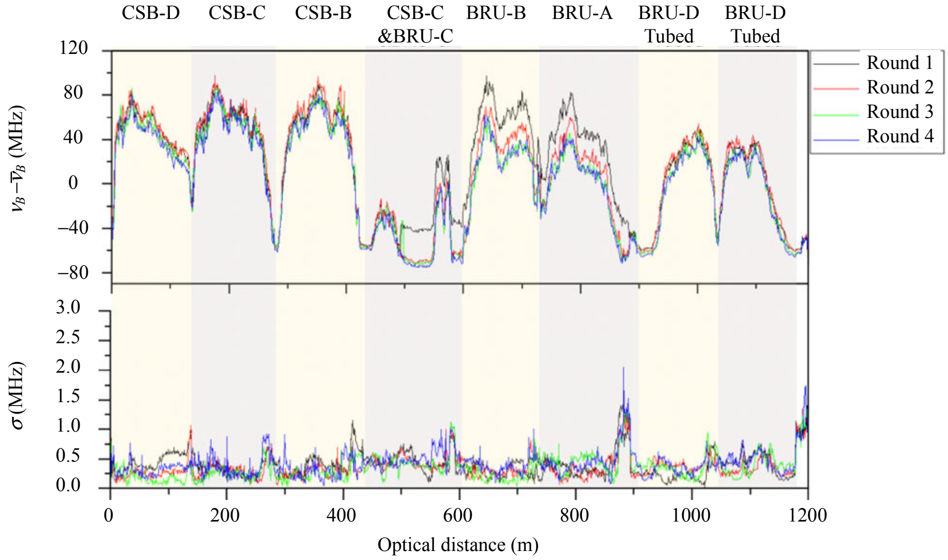

Fig. 6 Distributed BFS and its standard deviation of the four passing of the pulse through the systems measured in the July 2020 campaign.

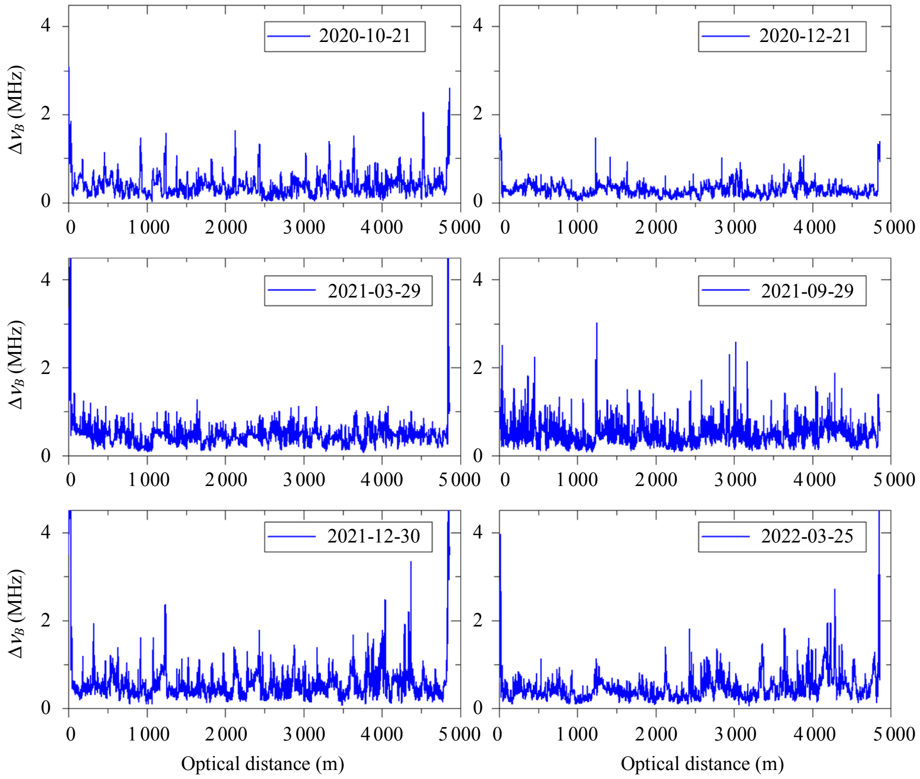

Fig. 7 Standard deviation of the BFS along the optical path for the measurements taken in each campaign.

Figure 6 shows the BFS measured along the fiber in the four rounds and averaged for the 10 measurements collected in each of the campaigns (date 2020-06-18). Each trace exhibits sharp changes at certain locations, revealing the presence of discontinuities in the optical path, mainly related to splices, while showing a continuous record along the distance for all the fiber spans. The bottom graph depicts the standard deviation (STD) of this dataset. It shows a steady value along the continuous fiber sections, which does not increase with the distance, indicating that the signal-to-noise ratio does not decrease with the distance. Discontinuities in the fiber can be easily detected by the greater standard deviation values than the average. This is due to the enhanced sensitivity of the fiber in splices and tight bends. When any of these two phenomena appears, there is a higher uncertainty in the calculations of the BFS. The latter graph is used to: 1) assess the repeatability of the measurement set, indicating whether there is any statically abnormal trace that has to be discarded; 2) set the strain resolution of the measurements. The average STD for the reference set taken in June 2020 was 0.77 MHz. Figure 7 shows the standard deviation for each campaign and their average values along the fiber. Conversion from BFS variation to the strain depends on the strain sensitivity of standard single-mode fibers, which is widely established at 0.05 MHz/με [12]. With this response coefficient, it can be determined that the system is operating with a maximum uncertainty of 18 με.

3.2 Spatial calibration

The accuracy of the location of the measurements is directly related to uncertainties in the refractive index of the fiber. Location errors propagate with a cumulative effect throughout the spatial-positioning calculations of the pulse based on its flight time. Nonetheless, an accurate characterization of the refractive index allows the precise positioning of the data along the fiber, rather than those in the monitored ground or infrastructure. This is because the length of the deployed fiber cable is greater than the linear distance covered by the cable in the ground or infrastructure. This difference can be related to multiple factors, such as the excess of the fiber cable to allow for re-splicing in case repairs are needed, sinuous traces and bends associated with multiple connected trenches, or the manholes hosting splices where spools of fibers are reserved. The most practical approach to resolve this positioning problem is to generate recordable stimuli at precisely determined positions that will serve as tie points for determining the spatial distribution of the data by linear interpolation.

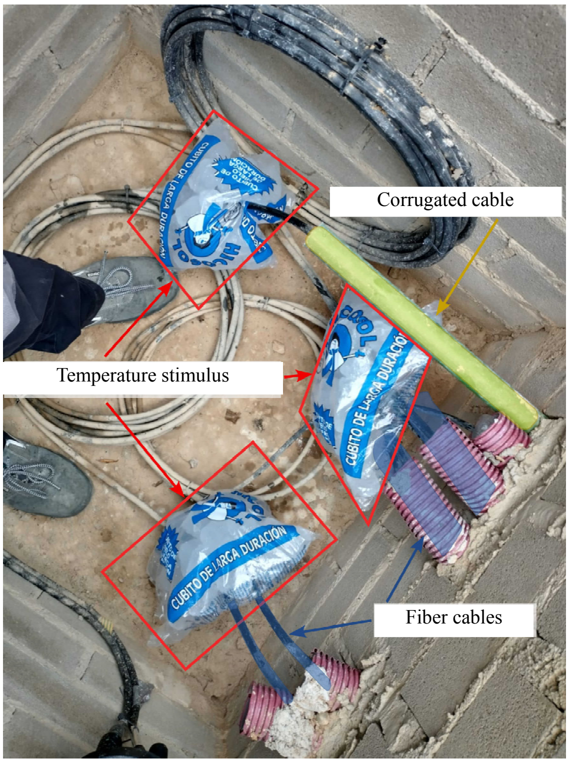

Fig. 8 Ice bags placed in a manhole to induce temperature variations in the cable.

In our case, we apply a thermal stimulus at specific and accessible points along the fiber. In particular, we place several ice bags in contact with cable spools inside the manholes, inducing a strong local drop in the temperature of the cable and the fiber. Once the bags are placed, the interrogator is set to acquire data until an obvious thermal change is detected. The exact location of the points where the cable is stimulated is easily determined by comparing the data recorded at the beginning and at the end of the experiment. Figure 9 depicts the variation of the BFS profile along the fiber between the first and the last measurements. The total time lapse between the measurements is 3 hours. Shaded areas in Fig. 9 delimit the section where the variation of the BFS is greater than the STD value determined in the absence of stimulus. Considering that, when placing the ice bags, this spot is the only section of the fiber affected by a significant stimulus, during the measurement period, these shaded areas represent the optical path within the manholes and thus will be excluded from the strain calculations. Note that this procedure makes it possible to remove the influence of the excessive fiber or splices in the manholes as it provides the exact position of the fiber at the exit of the manhole. This information enables the alignment of the different rounds of the pulse trip. By doing this, we get the strain of each cable four times and thus we can reduce the uncertainty in the displacement measurement.

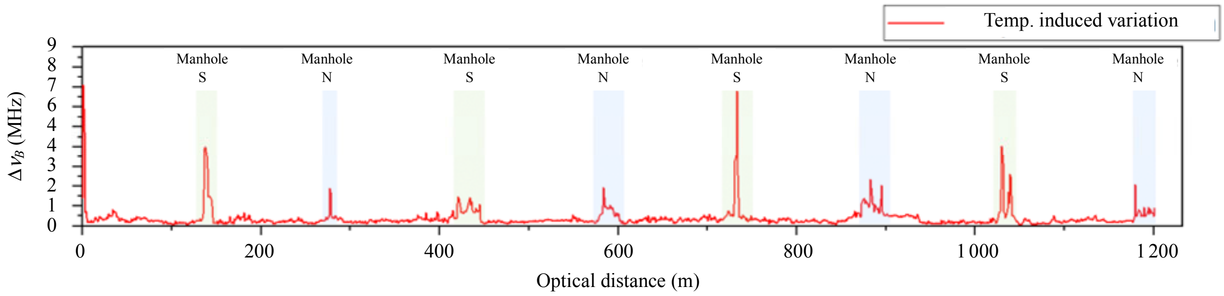

Fig. 9 BFS difference recorded throughout the spatial calibration campaign, showing the thermally-stimulated points at Manholes S and N.

4. Results and discussion

4.1 Measurement results

The first set of data was recorded in June 2020, which was established as the reference or initial condition of the fiber and thus of the terrain. Since then, 7 additional measurement campaigns were performed every 3 months covering a total time lapse of 21 months. Each measurement was obtained from the four rounds of the fiber path folded according to the spatial calibration detailed in the previous section. For the sake of brevity, we illustrate the results obtained in the cables deployed in Trenches C and B. It can be reasonably assumed that these cable sections are affected by a vertical displacement similar to that measured along the leveling lines.

Figure 10 shows the strain profiles of all the campaigns for the cable CSB-C installed in the upper level of Trench C [Fig. 1(d)]. The graph shows consistent strain profiles for all the campaigns with slight variations between them related to the continuous slow subsidence in the sinkhole. Positive and negative values record the limited axial strain of the sensor cable induced by local extension and contraction in the fiber affected by the sagging sinkhole, respectively. This strain pattern has been previously reported in laboratory calibration tests [24] and is consistent with deformation features observed in sagging sinkholes [27].

Figure 11 shows the strain for the cables CSB-B and BRU-B installed in Trench B: one above the other. Both cables exhibit analogous strain profiles, indicating the similar vertical displacement at different depths within the same trench. The slight difference between both cables can be related to different coupling of the fiber with the surrounding ground. The lower cable buried by thicker soil is expected to have better coupling with the surrounding ground.

In both figures, the strain data show similar spatial patterns and temporal evolution. It is worth noting a substantial increase in the negative strain occurred around 80 m–90 m between the campaigns 2021-09-29 and 2021-12-30. The timing of this local strain enhancement coincides with the Ebro River flood that peaked on 2021-12-14.

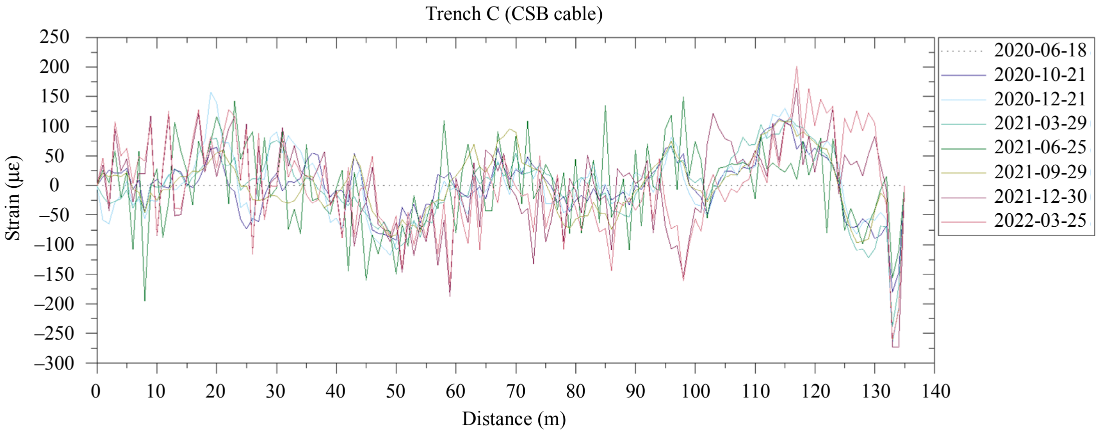

Fig. 10 Strain profiles recorded in all the campaigns along the cable CSB-C, installed in the upper level of Trench C.

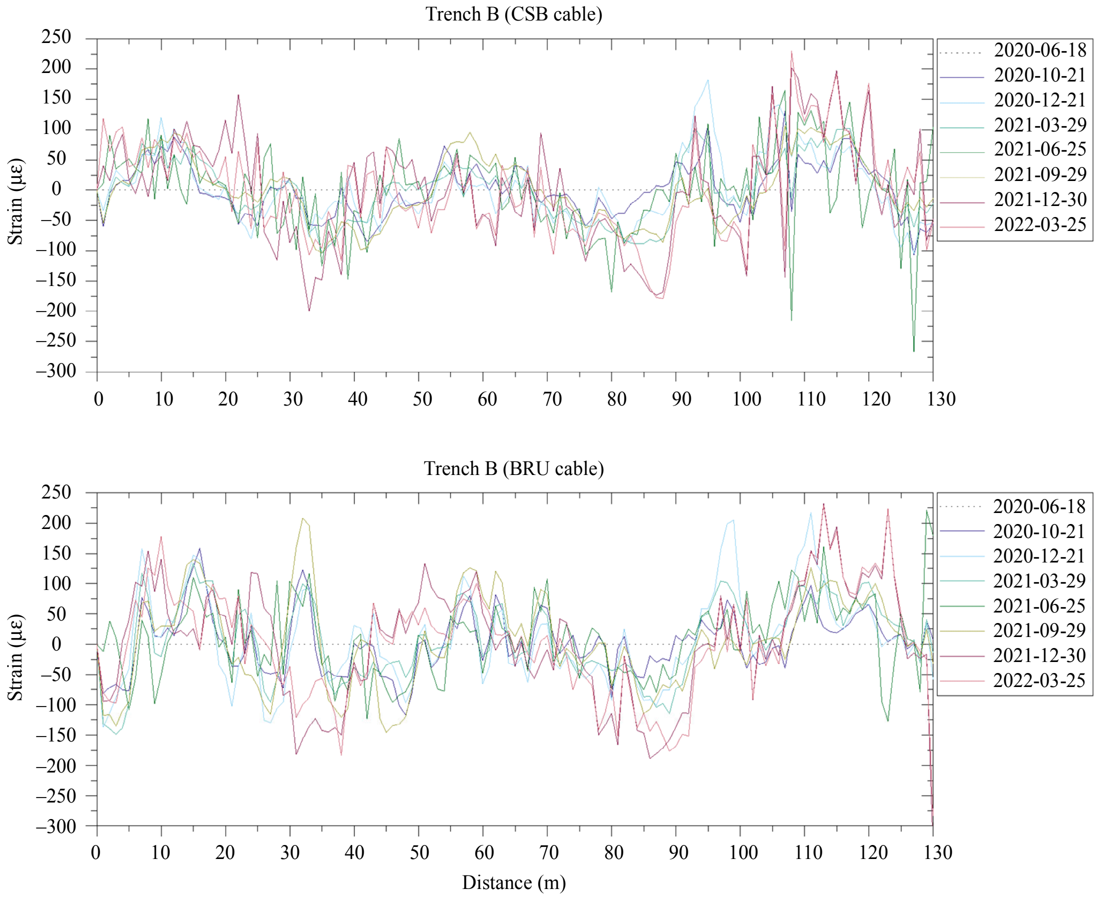

Fig. 11 Strain profiles recorded in all the campaigns along the cables CSB-B and BRU-B installed in Trench B.

4.2. Comparison to reference measurement

The performance of the BOTDA system can be assessed by comparing the strain and deformation profiles recorded by the fiber cables with the vertical displacement measured along the adjacent high-precision leveling lines.

Figure 12(a) shows the vertical displacement profiles obtained after applying (3) to the strain data measured in the cable BRU-B, while Fig. 12(b) depicts the same magnitude measured by high-precision leveling in the leveling line west. The BOTDA displacement profiles are aligned with the displacement profiles of the adjacent leveling line for comparison. The profiles derived from the BOTDA measurements show a good spatial correlation with the HPL data. Although the section corresponding to distance of 0 m–70 m indicates displacement values higher than those recorded with the leveling method, the data show the maximum displacement at 80 m–90 m, coinciding with the location where the leveling line records the maximum subsidence (Benchmark 12). At that position, the calculated displacement shows a maximum negative peak, which corresponds to negative strain values in the same region depicted in Fig. 11. This excessive displacement obtained with the BOTDA in the initial meters, 0 m to 70 m, can be originated from an incorrect evaluation of the displacement in the points close to the manhole. This would explain an overestimation in this region that does not affect the spatial profile of the recovered data, as it can be seen in the good correlation in the rest of the cable. This displacement profile across the cable is consistent with a sagging subsidence mechanism characterized by contraction in the inner part of the sinkholes and extension at the margins, as illustrated in Fig. 5. Terminal points of the cable correspond to the location of the manhole and thus present no vertical

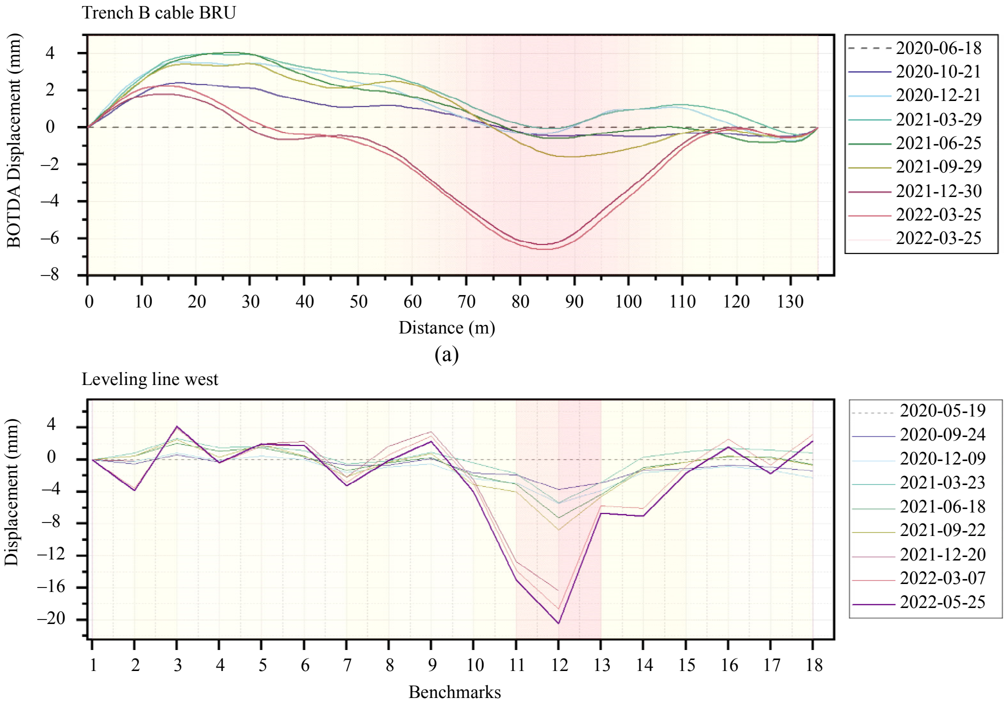

(a)

(b)

Fig. 12 Vertical displacement profiles: (a) obtained from the strain data measured in Trench B with the BRU cable throughout the different campaigns and (b) measured by high-precision leveling along the west line.

displacement. In the central region with the highest subsidence and contraction, the negative strain values show a substantial increase between September 2021 and December 2021, returning to the previous pattern between December 2021 and March 2022. This significant increase could be attributed to the Ebro River flood of December 2021, during which subsidence experienced a significant acceleration as indicated by the high-precision leveling data [Fig. 12(b)].

Figure 13(a) represents, for comparison: 1) the difference of the displacement calculated with the strain measured in the cable BRU-B in September 2021 and December 2021 (red line); 2) the average of the displacement difference between successive campaigns (blue line), excluding the interval indicated above. Figure 13(b) shows an equivalent pattern for the leveling line west. Both techniques show a substantial displacement increment centered around Benchmark 12 and the distance of 80 m in the cable section, contrasting with the limited variation observed along the cable during the rest of the campaigns. This indicates that the BOTDA measurements replicate the spatial and temporal subsidence patterns measured by high-precision leveling.

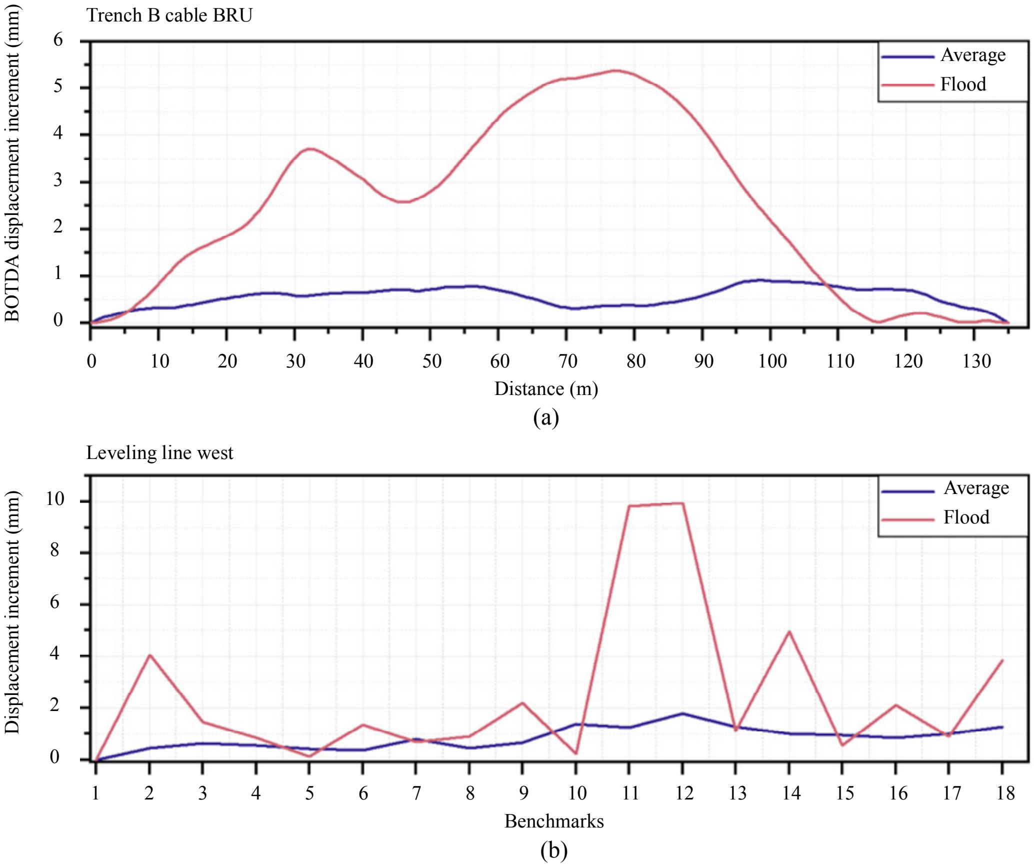

Fig. 13 Difference of the vertical displacement obtained from the strain in the cable BRU-B (a) and the HPL data in the west line (b) in the campaigns before and after the flood occurred in December 2021 (red), and the average difference from the rest of the intervals (blue).

Figure 14(a) shows the vertical displacement calculated with the BOTDA data recorded by the cable CSB-C, and Fig. 14(b) shows the vertical displacement profiles measured with the HPL technique along the leveling line east. Again, the BOTDA data show a good spatial and temporal correlation with the leveling data, with the maximum displacement around 80 m (aligned with Benchmark 12) and a displacement acceleration during the interval that includes the December 2021 flood. The profiles in the BOTDA display a ridge in the initial portion of the cable that can also be observed in the HPL data. Similar apparent uplift areas detected in the margins of active sinkholes by high-precision leveling have been attributed to flexural bulging [28]. This ridge seems to indicate the beginning of the subsidence area that in this case is wider than the one observed in Figs. 13(a) and 13(b). The lack of another ridge at the opposite margin of the subsidence area is related to the fact that the cable section does not cover completely the sinkhole, as the leveling data reveal, where the displacement profiles do not rise to null values on the right side of the graph [Fig. 14(b)].

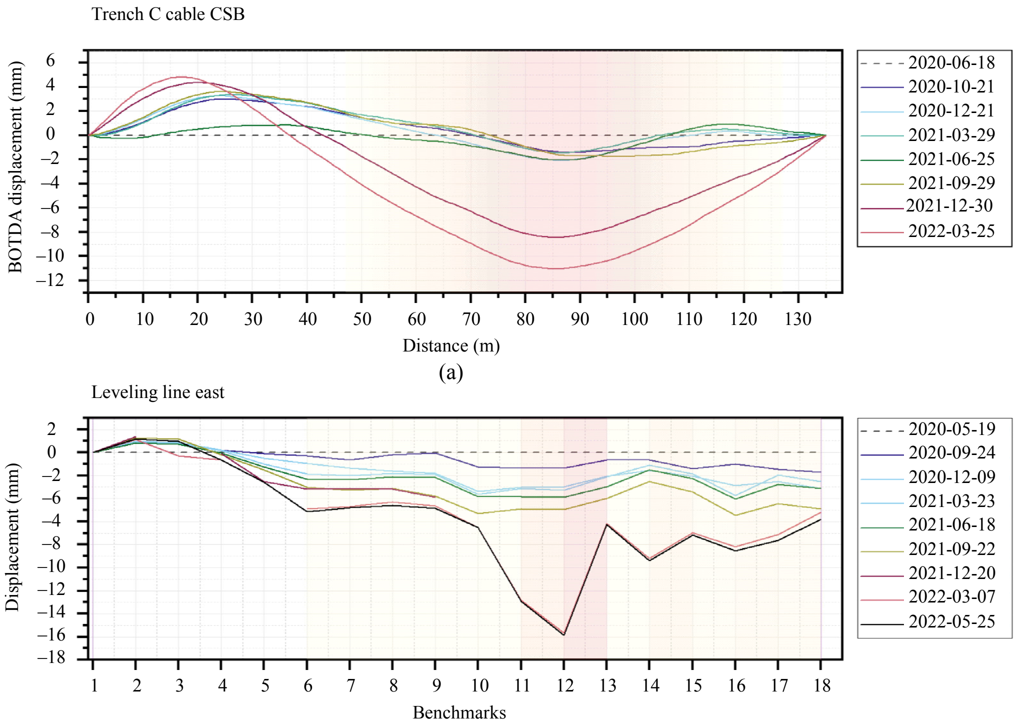

(a)

(b)

Fig. 14 Vertical displacement profiles: (a) obtained from the strain data measured in the cable CSB-C throughout the different campaigns and (b) measured in the leveling line east.

The differences in the displacement data obtained in the cable CSB-C and in the leveling line east between the campaigns before and after the flood, as well as the average of the difference in the rest of the time intervals is represented in Fig. 15. The BOTDA data show a clear displacement acceleration associated with the flood [Fig. 14(a)] similar to the leveling data [Fig. 14(b)]. Although both measuring techniques detect the maximum displacement at the same location, the section affected by the displacement in the BOTDA data is significantly wider. This deviation may be related to the non-ideal coupling between the fiber cable and the soil, resulting in some kind of lateral propagation of the strain effect.

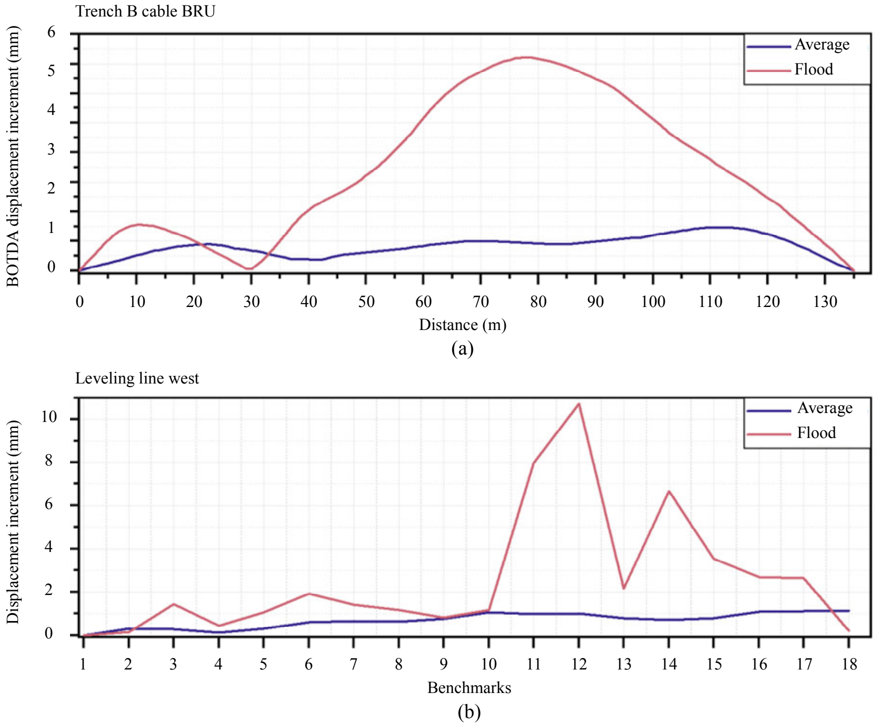

(a)

(b)

Fig. 15 Difference of the vertical displacement: (a) obtained from the strain recorded in the cable CSB-C and (b) measured by HPL data in the leveling line east between the campaigns before and after the flood occurred in December 2021 (red), and the average difference of the rest of the measurement intervals (blue).

5. Conclusions

In this paper, we have presented vertical displacement values calculated from strain measurements obtained with an enhanced BOTDA system in an active sinkhole. Compared to other scenarios, in which the technique has been tested, the monitored sinkhole is characterized by a large diffuse-edged subsidence area affected by very slow progressive subsidence (i.e., sagging sinkhole) that experiences phases of acceleration induced by flood events. This is a challenging scenario for the application of the BOTDA technique, not only because of the slowness of the ground deformation process, but also because of the very limited lateral displacement gradients. Nonetheless, with the deployed layout including several parallel fiber cables at different depths and precisely located by performing an on-site spatial calibration procedure, we have been able to reduce the uncertainties of the measurements. The cumulative vertical displacement of each point can be estimated through the integration of the strain values captured by the BOTDA. Despite the difficult scenario, the BOTDA data show a good spatial and temporal correlation with the subsidence values measured by the high-precision leveling. Although it is not possible to precisely delimit the edges of the subsidence area solely with the BOTDA data, there is a good coincidence in the position of the maximum subsidence zones and the phases of the enhanced deformation induced by flooding. The results of this study demonstrate that the BOTDA is a promising technique for the sinkhole subsidence measurement and for the developing early-warning systems with the ability to anticipate and prevent catastrophic collapses.

Acknowledgment

This work has been supported by Ministerio de Ciencia e Innovación, Gobierno de España (Grant Nos. CGL2017-85045-P, PID2021-123189NB-I00, and DI-17-09169) and Government of Aragón (Grant No. Reference Group T20_23R). Jorge Sevil has a predoctoral contract (Grant No. PRE2018-084240) co-financed by the Spanish Government and the European Social Fund (ESF). The authors are very grateful to the City Hall of Alcalá de Ebro and the Confederación Hidrográfica del Ebro for granting permission to install the monitoring system.

Declarations

Conflict of Interest The authors declare that they have no competing interests.

References

[1] Y. Liu, H. Li, Y. Wang, Y. Men, and Q. Xu, “Damage detection of tunnel based on the high-density cross-sectional curvature obtained using strain data from BOTDA sensors,” *Mechanical Systems and Signal Processing*, 2021, 158: 107728.

[2] H. Pei, J. Yin, and Z. Wang, “Monitoring and analysis of cast-in-place concrete bored piles adjacent to deep excavation by using BOTDA sensing technology,” *Journal of Modern Optics*, 2019, 66(7): 703–709.

[3] J. Xu, Y. Dong, Z. Zhang, S. Li, S. He, and H. Li, “Full scale strain monitoring of a suspension bridge using high performance distributed fiber optic sensors,” *Measurement Science and Technology*, 2016, 27(12): 124017.

[4] Z. Zhang, P. Guan, J. Xu, B. Wang, H. Li, and Y. Dong, “Horizontal loading performance of offshore wind turbine pile foundation based on DPP-BOTDA,” *Applied Sciences*, 2020, 10(2): 492.

[5] A. H. Hartog, *An Introduction to Distributed Optical Fibre Sensors*. Boca Raton: CRC Press, 2017.

[6] T. Horiguchi and M. Tateda, “BOTDA-nondestructive measurement of single-mode optical fiber attenuation characteristics using Brillouin interaction: theory,” *Journal of Lightwave Technology*, 1989, 7(8): 1170–1176.

[7] M. A. Soto, M. Taki, G. Bolognini, and F. D. Pasquale, “Optimization of a DPP-BOTDA sensor with 25 cm spatial resolution over 60 km standard single-mode fiber using Simplex codes and optical pre-amplification,” *Optics Express*, 2012, 20(7): 6860–6869.

[8] H. Su, Z. Wen, and P. Li, “Experimental study on PPP-BOTDA-based monitoring approach of concrete structure crack,” *Optical Fiber Technology*, 2021, 65: 102590.

[9] F. Gutiérrez, “*Sinkhole hazards*,” in Oxford Research Encyclopedia of Natural Hazard Science, Oxford: Oxford University Press, 2016: 1–92.

[10] F. Gutiérrez, A. Benito-Calvo, D. Carbonel, G. Desir, J. Sevil, J. Guerrero, *et al.*, “Review on sinkhole monitoring and performance of remediation measures by high-precision leveling and terrestrial laser scanner in the salt karst of the Ebro valley, Spain,” *Engineering Geology*, 2019, 248: 283–308.

[11] D. Culverhouse, F. Farahi, C. N. Pannell, and D. A. Jackson, “Stimulated Brillouin scattering: a means to realise tunable microwave generator or distributed temperature sensor,” *Electronics Letters*, 1989, 25(14): 915–916.

[12] T. Horiguchi, T. Kurashima, and M. Tateda, “Tensile strain dependence of Brillouin frequency shift in silica optical fibers,” *IEEE Photonics Technology Letters*, 1989, 1(5): 107–108.

[13] H. Ohno, H. Naruse, M. Kihara, and A. Shimada, “Industrial applications of the BOTDR optical fiber strain sensor,” *Optical Fiber Technology*, 2001, 7(1): 45–64.

[14] Z. Zhou, J. He, K. Yan, and J. Ou, “Fiber-reinforced polymer-packaged optical fiber sensors based on Brillouin optical time-domain analysis,” *Optical Engineering*, 2008, 47(1): 014401.

[15] C. K. Y. Leung, K. T. Wan, D. Inaudi, X. Bao, W. Habel, Z. Zhou, *et al.*, “Review: optical fiber sensors for civil engineering applications,” *Materials and Structures*, 2013, 48(4): 871–906.

[16] H. Chen, J. He, Y. Xue, and S. Zhang, “Experimental study on sinkhole collapse monitoring based on distributed Brillouin optical fiber sensor,” *Optik*, 2020, 216: 164825.

[17] Y. Dong, X. Bao, and L. Chen, “High-axial-resolution distributed lateral displacement measurement based on differential pulse-width pair BOTDA,” in *21st International Conference on Optical Fiber Sensors*, Ottawa, 2011, pp. 1482–1485.

[18] H. Wu, H. H. Zhu, C. C. Zhang, G. Y. Zhou, B. Zhu, W. Zhang, *et al.*, “Strain integration-based soil shear displacement measurement using high-resolution strain sensing technology,” *Measurement*, 2020, 166: 108210.

[19] H. Sang, H. H. Zhu, C. C. Zhang, G. Y. Zhou, B. Zhu, W. Zhang, *et al.*, “Strain distribution based geometric models for characterizing the deformation

of a sliding zone," *Engineering Geology*, 2019, 263: 105300.

[20] D. Hauswirth, M. Iten, and A. M. Puzrin, "Detection of ground movements using soil-embedded distributed fiber optic sensors," in *Geotechnical and Geophysical Site Characterization : Proceedings of the 4th International Conference on Site Characterization ISC-4*, Basel, Switzerland, 2013, pp. 579–586.

[21] S. P. Liu, B. Shi, K. Gu, C. C. Zhang, J. L. Yang, S. Zhang, *et al.*, "Land subsidence monitoring in sinking coastal areas using distributed fiber optic sensing: a case study," *Natural Hazards*, 2020, 103(3): 3043–3061.

[22] K. Gu, B. Shi, C. Liu, H. Jiang, T. Li, and J. Wu, "Investigation of land subsidence with the combination of distributed fiber optic sensing techniques and microstructure analysis of soils," *Engineering Geology*, 2018, 240: 34–47.

[23] Y. Peled, A. Motil, I. Kressel, and M. Tur, "Monitoring the propagation of mechanical waves using an optical fiber distributed and dynamic strain sensor based on BOTDA," *Optics Express*, 2013, 21(9): 10697–10705.

[24] J. Liu, Y. Wang, Y. Lu, J. Wei, and D. P. Kanungo, "Application of distributed optical fiber sensing technique in monitoring the ground deformation," *Journal of Sensors*, 2017, 2017: e6310197.

[25] A. Benito-Calvo, F. Gutiérrez, A. Martínez-Fernández, D. Carbonel, T. Karampaglidis, G Desir, *et al.*, "4D monitoring of active sinkholes with a terrestrial laser scanner (TLS): a case study in the evaporite karst of the Ebro valley, NE Spain," *Remote Sensing*, 2018, 10(4): 571.

[26] A. Domínguez-López, A. López-Gil, S. Martín-López, and M. González-Herráez, "Signal-to-noise ratio improvement in BOTDA using balanced detection," *IEEE Photonics Technology Letters*, 2014, 26(4): 338–341.

[27] J. De Waele and F. Gutiérrez, *Karst Hydrogeology, Geomorphology and Caves*, Hoboken: Wiley-Blackwell*,* 2022.

[28] J. Sevil, F. Gutiérrez, C. Carnicer, D. Carbonel, G. Desir, Á. García-Arnay, *et al.*, "Characterizing and monitoring a high-risk sinkhole in an urban area underlain by salt through non-invasive methods: detailed mapping, high-precision leveling and GPR," *Engineering Geology*, 2020, 272: 105641.